

Stimulated emission depletion (STED) nanoscopy of a fluorescent protein-labeled organelle inside a living cell

Birka Hein, Katrin I. Willig, and Stefan W. Hell*

Department of Nanobiophotonics, Max Planck Institute for Biophysical Chemistry, 37070 Göttingen, Germany

We demonstrate far-field optical imaging with subdiffraction resolution of the endoplasmic reticulum (ER) in the interior of a living mammalian cell. The diffraction barrier is overcome by applying stimulated emission depletion (STED) on a yellow fluorescent protein tag. Imaging individual structural elements of the ER revealed a focal plane (x, y) resolution of <50 nm inside the living cell, corresponding to a 4-fold improvement over that of a confocal microscope and a 16-fold reduction in the focal-spot cross-sectional area. A similar gain in resolution is realized with both pulsed- and continuous-wave laser illumination. Images of highly convoluted parts of the ER reveal a similar resolution improvement in 3D optical sectioning by a factor of 3 along the optic axis (z). Time-lapse STED recordings document morphological changes of the ER over time. Thus, nanoscale 3D imaging of organelles in the interior of living cells greatly expands the scope of light microscopy in cell biology.

The green fluorescent protein (GFP) and its derivatives have revolutionized the imaging of living cells by providing specific labeling of proteins through genetic fusion (1). Similarly, confocal fluorescence microscopy stands out by the fact that it provides 3D optical sectioning and low-background detection (2). Both developments have greatly facilitated the noninvasive exploration of living cells in three dimensions. However, as for any standard far-field optical microscope, the resolution of a confocal microscope is limited by diffraction to $\approx \lambda/(2 \text{NA})$, with λ denoting the wavelength of light and NA denoting the numerical aperture of the lens (3). By breaking the diffraction barrier and providing subdiffraction resolution, stimulated emission depletion (STED) microscopy (4, 5) has altered long-standing notions about the resolving power of light microscopy and, thus, initiated a hot topic of research at the interface of physics, chemistry, and biology (6).

In a typical implementation of a scanning STED microscope, a diffraction-limited spot of excitation light is overlaid with a red-shifted doughnut-shaped beam for STED (5). The wavelength of the STED beam is tuned to the red edge of the emission spectrum of the fluorescent marker so that it is able to deexcite the potentially excited molecules through stimulated emission. As a result, the doughnut-shaped STED beam prevents the effective excitation of the marker molecules in the focal-spot area except for those that happen to be located in its central area. If I_s denotes the dye-wavelength characteristic intensity at which the fluorescence excitation is reduced to half, for intensities $I \gg I_s$ of the STED beam, the ability of a molecule to fluoresce is essentially switched off. Therefore, applying an intensity of $I \gg I_s$ at the doughnut crest confines the fluorescence to a spot of diameter (7)

$$\Delta r \approx \lambda/2\text{NA} \sqrt{1+I/I_s}. \quad [1]$$

By applying $I/I_s \gg 1$, the effective focal spot can be substantially reduced, in principle, down to the size of a molecule or even

further to submolecular dimensions. Scanning this spot through the sample allows the sequential recording of features that are as close as Δr , thus automatically rendering images with subdiffraction resolution Δr . The spatial confinement of the fluorescence spot to Δr is purely physical in nature and, in principle, unlimited by diffraction.

STED microscopy and its derivatives based on switching photoactivatable proteins (8) were complemented recently by powerful methods based on the sequential stochastic switching of individual photoactivatable fluorophores in wide-field illumination (9–11). The photochromic molecules are switched to a conformational state, leading to $m \gg 1$ consecutive photon emissions, allowing the calculation of the position of individual fluorophores. Similar to STED microscopy (12), these methods have been demonstrated with both fluorescent proteins (9) and synthetic organic fluorophores (10), but because they assemble the images molecule by molecule, they have so far been bound to relatively long recording times. Besides, although they can provide superresolution along the z axis (13), single-molecule switching methods do not provide optical sectioning unless the switching is effected by a nonlinear multiphoton absorption (14). Therefore, they cannot readily address an arbitrary focal plane in the interior of a sample. This limitation also accounts for the fact that, unlike with STED microscopy (5), live cell recordings with these methods have so far been largely limited to the plasma membrane (15).

In contrast, by taking advantage of its ability to target arbitrary coordinates within a cell and to record many molecules from those coordinates in parallel, STED microscopy has been shown to capture the movement of synaptic vesicles inside living neurons at video rate (16). However, in these recordings, the proteins of interest were labeled with secondary antibodies tagged with organic fluorophores, a labeling procedure whose application in living cells is severely limited. Here we report STED microscopy in the interior of a living cell by using a fluorescent protein (17) as an indicator. Specifically, we demonstrate a lateral (all physics-based) resolution of 50 nm in time-lapse recordings of its endoplasmic reticulum (ER). Moreover, we attain a 3-fold improvement in optical sectioning or z resolution over that of a confocal microscope by squeezing the focal fluorescent spot along the z axis; this subdiffraction-sized focal spot can be freely targeted within a living cell. Finally, we show in this application that a cost-effective continuous-wave

Author contributions: S.W.H. designed research; B.H. and K.I.W. performed research; B.H. and K.I.W. analyzed data; and B.H., K.I.W., and S.W.H. wrote the paper.

The authors declare no conflict of interest.

Freely available online through the PNAS open access option.

*To whom correspondence should be addressed at: Department of NanoBiophotonics, Max Planck Institute for Biophysical Chemistry, Am Fassberg 11, 37077 Göttingen, Germany. E-mail: shell@gwdg.de.

This article contains supporting information online at www.pnas.org/cgi/content/full/0807705105/DCSupplemental.

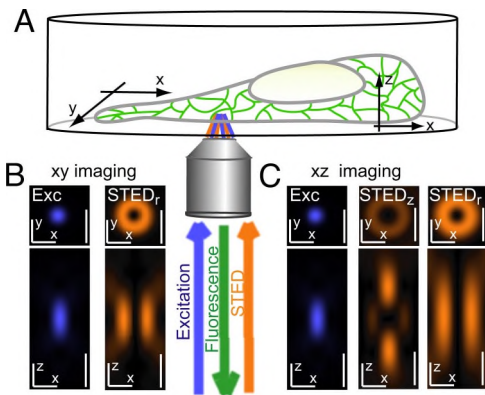


Fig. 1. Schematic showing the use of the excitation and deexcitation (STED) beams for 3D STED imaging inside a living cell. (A) An objective lens focuses the beams (blue, excitation; orange, STED) into the ER while also collecting the resulting beam of fluorescence photons. Images are acquired by translating the focused laser beams through the cell. (B) *xy* imaging: excitation spot (blue) and cylindrically shaped focal spot (orange) for stimulated emission, squeezing the fluorescent spot in the *xy* plane (STED_r, or r-doughnut). Both the lateral (*x*, *y*) cross-sections in the focal plane and the axial cross-section (*x*, *z*) are shown (Upper and Lower, respectively). (C) *xz* imaging: excitation spot (blue) and STED spot composition consisting of a spot featuring a maximum above and below the focal plane along the *z* axis, referred to as STED_z, plus an enlarged r-doughnut STED_r. All spots represent data calculated by using the experimental conditions applied. (Scale bars, 500 nm.)

(CW) fiber laser for STED yields a resolving power that is comparable to the one provided by a complex laser system, thus opening a simple and economic pathway to 3D-fluorescence nanoscopy of the living cell interior.

Results

Mammalian cells (PtK2 line) were grown on a coverslip and transfected with a plasmid encoding the yellow fluorescent protein (YFP) Citrine (17) targeted to the ER. Citrine is a variant of GFP with an excitation and emission spectrum similar to that of the YFP. After at least 24 h of incubation, cover glasses with the transfected cells were transferred to a home-built microscope chamber and placed on an inverted STED microscope (Fig. 1A) featuring an oil-immersion lens with an NA = 1.4. The medium was exchanged with Dulbecco's modified Eagle's medium (DMEM) containing no phenol red. The absorption of Citrine peaks at 516 nm, whereas the fluorescence occurs primarily between 520 and 570 nm. In the pulsed-illumination variant of STED microscopy, we excited the fluorophore with 100-ps pulses at $\lambda = 490$ nm originating from a pulsed-laser diode operating at 80 MHz (Picoquant). The pulses for STED were provided by an optical parametric oscillator (APE) tuned to 595 nm, which is at the red edge of the emission spectrum of the fluorescent protein. The pulses from the oscillator also provided the trigger for the excitation laser diode. The fluorescence was collected by the objective lens and imaged onto a confocal pinhole, the diameter of which corresponded to $\approx 78\%$ of a back-projected focal Airy disk. Confocalization is not required in STED microscopy, but it conveniently provides background suppression and optical axial sectioning. In addition, blocking the STED beam allows one to directly compare the subdiffraction resolution with the gold standard in far-field optical microscopy (i.e., that of confocal microscopy).

The sample was mounted on a piezoelectric translation stage capable of scanning the sample in the *x*, *y*, and *z* directions. Scanning the sample with respect to the stationary beams and recording the fluorescence intensity for each coordinate assembled an image or a series of images. A home-built sample holder enabled heating of the cell while being imaged. However, except

for faster movements, we did not observe significant differences in the ER morphology with the temperature. Therefore, we imaged at room temperature, within 30 min after removing the cells from the incubator. All *xy* images were recorded with a pixel size of 20 nm in the *x* and *y* directions, whereas scanning along the *z* axis was performed with a 60-nm pixel size.

To accommodate for the structures to be imaged, the microscope was set up for two different modalities to squeeze the fluorescence focal spot. Fig. 1B shows a cylindrical STED focal intensity distribution forming a doughnut in the focal (*x*, *y*) plane (12), confining the spot in all radial directions in the focal plane; we refer to it as the r-doughnut or STED_r. The resulting effective focal spot of the STED microscope features a confocal axial sectioning that is suitable for structures that are not stacked more densely than ≈ 500 nm along the *z* axis. For imaging convoluted structures in 3D, we implemented the STED spot shown in Fig. 1C (5). Termed the z-doughnut or STED_z, this focal intensity distribution compresses the fluorescence spot primarily along the *z* axis. We applied it in conjunction with an enlarged r-doughnut that prevented fluorescence in the higher-order side lobes of diffraction of the excitation spot.

First, we imaged the ER of a living PtK2 cell in the pulsed mode, applying the r-doughnut of Fig. 1B. The time-averaged focal power of the STED beam was 16.3 mW, spread across the area of the doughnut. By turning on and off the STED beam in every line in the *x* direction, we simultaneously recorded the STED image and the confocal reference. Whereas in the confocal reference (Fig. 2A) mainly large areas can be seen (compare arrowheads), the STED image (Fig. 2B) reveals the polygonal network of the living-cell ER, distinguishing single tubules or ER elements. The smallest details in the image were in the range of ≈ 52 -nm full width at half maximum (FWHM) as shown in Fig. 2C. Because it includes the finite dimensions of this smallest feature, this FWHM represents a lower bound of the resolving power of the system (i.e., $\Delta r < 50$ nm). For comparison, confocal imaging results in a structure of ≈ 210 nm. In many cases, the ER tubules are significantly larger than 50 nm in extent, in which case the STED image largely reproduces the actual ER network. Note that the decrease in focal-spot diameter amounts to a 16-fold reduction in area of the cross-section of the effective spot in the focal plane.

Because the same pixel dwell time (0.05 ms) is used in the line-by-line comparison between the confocal and the STED recording (Fig. 2, A vs. B), the smaller spot diameter Δr of the latter causes the STED images to be darker than their confocal counterparts. Yet, their content in information is substantially improved, because the photons are collected from a more localized area in space. Taking advantage of the fact that Δr can be adjusted by regulating the focal intensity *I* of the STED beam, we repeatedly recorded images with different *I* and evaluated the FWHM of single well-separated ER tubules. As shown in Fig. 2D, the measured FWHM of the tubules decreases with increasing intensity *I* following the inverse square-root law formulated in Eq. 1. However, for the two largest intensity values, the FWHM is unchanged within the error of measurement, which indicates that the measured FWHM largely represents the actual size of that particular ER tubule or element (i.e., ≈ 50 nm).

Alternatively, we calculated the resolution of the STED microscope obtained with Citrine directly by using Eq. 1. To this end, we determined I_c through measuring the fluorescence inhibition on single ER tubules with increasing time-averaged power (and, hence, intensity) of a regularly focused pulsed-STED beam. At a time-averaged power $P_s = 0.9$ mW of the 80-MHz pulsed focal STED beam, the fluorescence had dropped by half, which corresponds to a pulse peak intensity $I_s = 81.2$ MW/cm². Hence, for the highest pulse peak intensity applied, $I = 807$ MW/cm², we obtain $\Delta r = 48$ nm. The compatibility with living cells is not surprising, because this intensity is ≈ 300 -fold

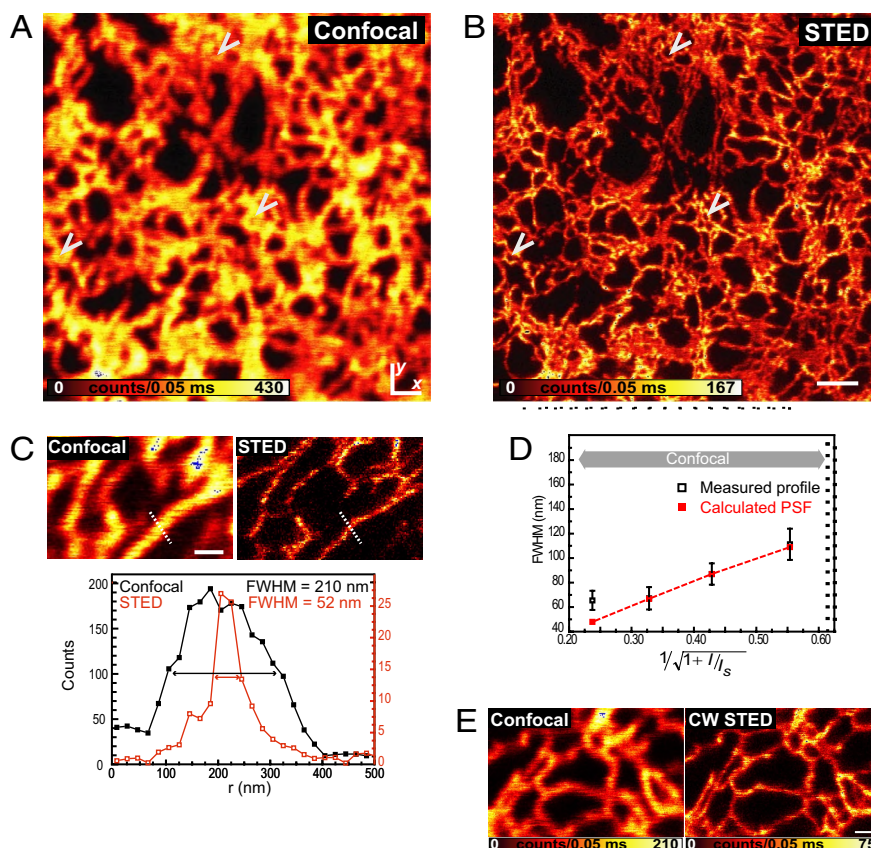


Fig. 2. Subdiffraction-resolution imaging of the ER in a living mammalian cell. Shown are confocal (A) and simultaneously recorded (B) STED (x, y) images from the ER marked by the fluorescent protein Citrine targeted to the ER (raw data: 16.3-mW STED focal intensity). (Scale bar, 1 μm .) The arrows point out rings formed by the tubular network of the ER, which are visible only in the STED image. (C) Confocal and corresponding STED image revealing features of 52-nm FWHM as indicated by the profile below (raw data: 35.7-mW STED focal intensity), indicating that the lateral resolution in the STED image is <50 nm. (Scale bar, 500 nm.) (D) FWHM of the calculated effective STED point-spread function (PSF) and of the measured profile of an ER tubule versus the inverse of the square root of the STED beam intensity I (see Eq. 1). The measured FWHM values are based on 125 line profiles measured per individual value I in 5 different images; the error bars represent the quadratic mean of the respective SDs. For lower STED intensities I , the measured size of the ER elements decreases with the sharpening of the PSF, as expected from the square-root law, whereas for FWHM of ≈ 60 nm, no further decrease in the FWHM is observed, implying that the ER elements are, on average, ≈ 60 nm in width. (E) Confocal and corresponding STED image recorded with CW laser beams of 3 μW for excitation and 112 mW for STED (592-nm wavelength) at the sample, revealing tubules as small as 60 nm by STED. (Scale bar, 500 nm.)

lower than the typical 200 GW/cm^2 required to effectively generate signal in a multiphoton microscope (18), which has become a standard tool for imaging living cells. The significantly longer duration of the STED pulse (300 vs. ≈ 0.3 ps) implies pulse energies that are of the same order or only slightly higher. It works to the advantage of STED that photoinduced damages are primarily caused by multiphoton absorption effects that scale quadratically or even cubically with the intensity (19). By contrast, stimulated emission is a single-photon phenomenon, the efficiency of which depends just on the number of photons that are present within the lifetime of the excited state.

For this reason, the peak intensity of the STED beam can be reduced with respect to the values shown above by implementing CW beams (20). As a rule of thumb, the affordable reduction of peak intensity is largely the ratio given by ≈ 300 -ps duration of the STED pulses over the lifetime of the excited state of the protein (3.6 ns) (i.e., by 12-fold). In CW operation, the excitation and deexcitation of the fluorophore cannot be separated in time, as is the case with pulses. Apart from this disadvantage, CW operation greatly simplifies the implementation of STED microscopy because it makes pulse preparation and timing inherently redundant. In particular, it allows the implementation of economical laser sources. For the excitation of the YFP Citrine, the pulsed diode was substituted by a simple CW laser diode (488

nm, Cobolt), whereas the CW beam for STED was delivered by a small-footprint fiber laser system (MPB Communication) emitting at $\lambda = 592$ nm. Focusing 112 mW of the latter to a doughnut-shaped area (which is approximately four times larger than a regularly focused spot) provided a CW intensity of $I = 62$ MW/cm^2 at the doughnut crest. Images with a resolution close to that obtained with the pulsed lasers were obtained by using the CW lasers. Fig. 2E shows ER tubules imaged with the CW-STED microscope to be as small as ≈ 60 nm in FWHM, indicating a >3 -fold improvement in lateral resolution over that of confocal microscopy.

For imaging structures that are strongly folded in 3D, it is necessary to overcome the diffraction barrier along the z axis as well, which can be accomplished by implementing the STED spot shown in Fig. 1C. To verify the improvement in the axial resolution, a part of the ER close to the nucleus was imaged. Because the effective focal spot functions as a noninvasive 3D probe, the improvement in z resolution also yields an improvement in optical sectioning. The resulting Fig. 3A exposes tubules stacked above each other, as well as other tubules diving up and down in the z direction. In contrast, the corresponding confocal image (Fig. 3B) cannot distinguish interconnected elements from those that are just stacked along the z axis. Fig. 3C shows a profile of a single ER tubule along the z axis evidencing an axial

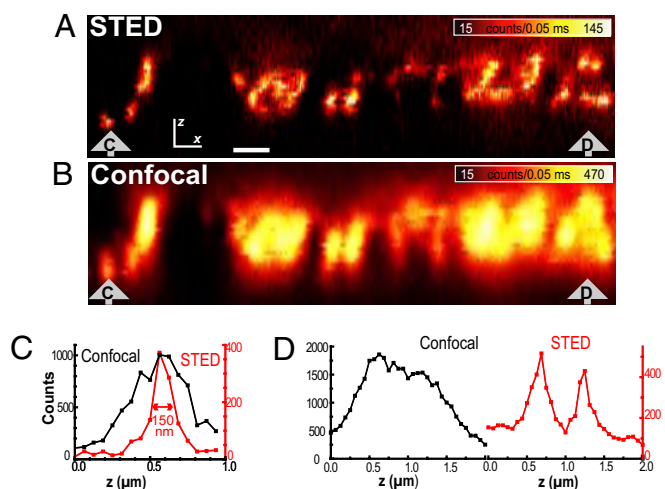


Fig. 3. Axial superresolution and improvement of optical sectioning inside a living cell using STED. An axial STED image (xz) of densely packed ER tubules (A) imaged by STED microscopy reveals single, stacked (oval) tubules, whereas in the confocal image (B), the same substructure is not revealed. The average focal power of the pulsed beams was $3 \mu\text{W}$ for excitation and 14.7 mW for the r-doughnut and 12.7 mW for the z-doughnut. (Scale bar, 500 nm .) (C) Line profile along the z direction (sum of four lines) of a single ER tubule at the marked position of the STED (A) and the confocal (B) images, respectively, revealing an axial FWHM of 450 nm in the confocal reference and 150 nm in the STED image. (D) Intensity profile along the z axis (sum of four z profiles) demonstrates the ability of the STED microscope to discern features that cannot be separated in the confocal reference.

resolution and optical sectioning of 150 nm of the STED microscope, which represents a 3-fold improvement over the 450-nm optical sectioning of the confocal microscope. We note that the reported improvement in resolution is purely based on optically switching off the fluorescence ability of the YFP by STED.

Next, we visualized the movement of the ER with $\approx 50\text{-nm}$ lateral resolution (Fig. 4) by recording consecutive images $10 \times 2.5 \mu\text{m}$ in size (512×128 pixel) with a 10-s frame rate and a pixel dwell time of $50 \mu\text{s}$. The time series of images in Fig. 4 and supporting information (SI) Movie S1 vividly reveals the structural changes of the ER network, such as the forming and vanishing of enclosures. Furthermore, this setup could be used for manipulating the cells through adding agents or by changing the temperature. For example, addition of $5 \mu\text{g/ml}$ Filipin III, a drug that breaks down the ER in living cells, resulted in fragmentation of the ER to large, fast-moving enclosures.

Discussion, Conclusion, and Outlook

The reason for selecting a stage-scanning system was the fact that it enabled a simple implementation of the concept, allowing convenient interchange of optical elements such as filters and dichroic mirrors. The xy images shown in Fig. 3 were recorded by unidirectional scanning along the x axis and then shifting the sample stage by the size of a pixel in the y direction. Images of typical $10 \times 2.5\text{-}\mu\text{m}$ size were obtained with an image frame rate of 10 s , whereby more than half of this period was attributable to a recording dead time necessitated by the return of the stage for each line. Because of the movement of the ER in the interim period, some ER elements appear slightly shifted between two consecutive lines. Replacing the stage-scanning system with a much faster beam-scanning modality or implementing arrays of STED beam zeros will enable real-time imaging of the ER and the recording of 3D data stacks from the ER within seconds. The reduction in signal resulting from the decreased pixel dwell time can be partially compensated by a larger excitation beam power

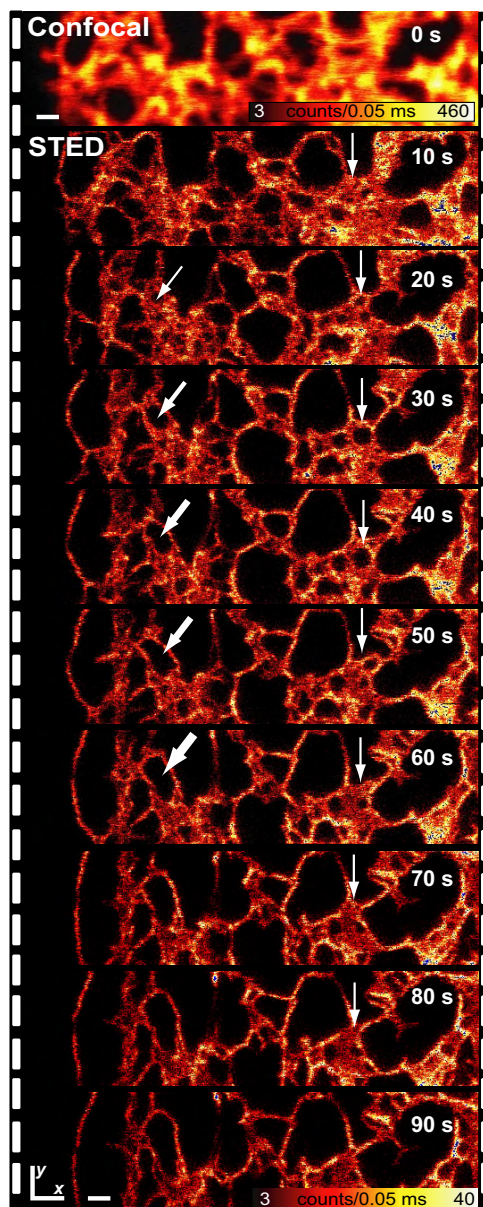


Fig. 4. Dynamics of the ER imaged with subdiffraction resolution by STED (see also Movie S1). The images (10-s recording time each) were recorded consecutively, showing the movement of the ER with a resolution of $\approx 50 \text{ nm}$. The first image (time point 0 s) is a confocal reference image. The arrows indicate structural changes during the recording of the movie. (Scale bar, 500 nm .)

(here only $\approx 3 \mu\text{W}$) while keeping the STED intensity unchanged.

The fluorescent protein was fused to an ER-targeting signal and an ER-retention signal, giving rise to free diffusion in the ER. Because of the fast exchange of potentially photobleached proteins from the imaged area within the whole ER network, we could not observe a decrease in brightness over the 9 STED recordings shown in Fig. 4. We recorded up to 30 STED images before we saw morphological changes of the ER network; the exact number differed from cell to cell. To investigate whether the STED imaging shown herein is restricted to freely diffusing proteins, we imaged Citrine-labeled microtubules of a living PtK2 cell with a resolution of 60 nm (Fig. 5). Although diffusion is excluded in this case, several images of the same

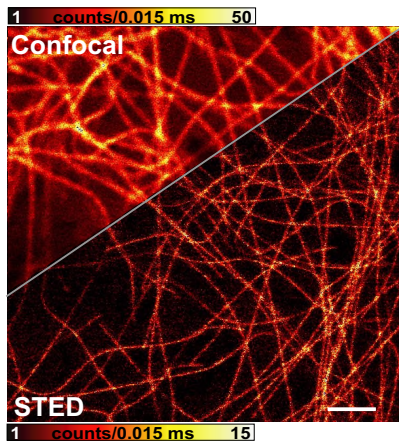


Fig. 5. Subdiffraction resolution fluorescence imaging of Citrine-labeled microtubules inside a living PtK2 cell. In both the confocal reference and the STED counterpart, excitation was performed in the pulsed mode with $7.6 \mu\text{W}$ of time-averaged focal power. In the STED mode, a STED beam of 31-mW average power was added, which improves the lateral resolution inside the living cell from 180 to 60 nm. The resolution improvement is purely physical in nature (i.e., obtained without mathematical processing of recorded data); this attribute holds for all of the data shown in the article. (Scale bar, $2 \mu\text{m}$.)

area could be recorded. Nonetheless, photobleaching is more relevant in this case than in samples in which the protein is able to diffuse, calling for further improvements of the photostability of fluorescent proteins or improved illumination schemes.

As opposed to the 1.4-NA oil-immersion lenses used, the use of 1.2-NA water lenses would have provided an even deeper penetration depth along the z axis, because the matching of the refractive index of the immersion liquid with that of the medium of the cell avoids spherical aberration induced by the refractive index mismatch. Likewise, because the semiaperture angle of a 1.4-NA oil-immersion objective is $\alpha = 68^\circ$ and, therefore, slightly larger than that of a similar water-immersion objective ($\alpha = 64^\circ$), some of the laser light is lost because of total internal reflection on the interface between the cover glass and the aqueous medium. On the other hand, the number of collected photons is larger with the oil-immersion lens because of the larger collection angle. In our case, spherical aberrations resulting from mismatch of the refractive index were minor because the imaged structure was relatively close (a few micrometers) to the coverslip. To validate this assumption, we also imaged the ER with an NA = 1.2 water-dipping lens (Fig. S1), in which case images similar to those shown in Figs. 2 and 4 were obtained.

Because a typical STED microscope can be operated as an ordinary scanning (confocal) microscope, long-time temperature controls and temperature ramps can be readily implemented. Dedicated sample chambers provide the possibility of manipulating the sample like in any other standard light microscope. Because it requires dichroic filter sets similar to those for the fluorescent protein Citrine, we also investigated the use of the enhanced YFP (EYFP). We obtained the same resolution and brightness in the images of the EYFP-labeled samples.

The resolution gain demonstrated throughout this article stems from the interaction of the fluorescent protein label with the light. No mathematical processing of the image data were applied, which should facilitate the further use of the data, for example, for quantitative spectroscopic evaluations. The resolution conveyed in the images can be further augmented by applying linear or nonlinear deconvolution algorithms.

In conclusion, we have demonstrated the imaging of the ER with subdiffraction resolution in the interior of a living cell by applying STED on YFPs. A 4-fold all-optical improvement in resolution was gained in all lateral directions, whereby the 3-fold increase in axial resolution also represents a 3-fold improvement in optical sectioning. In particular, we deduce that many ongoing microscopy studies in living cells that are currently performed with a diffraction-limited confocal microscope can be carried out with a substantially improved spatial resolution in all directions by means of STED microscopy.

Materials and Methods

STED Microscopy. A schematic of the STED microscope is shown in Fig. S2. In the pulsed version of STED, the excitation pulses at 490-nm wavelength and 100-ps duration were delivered by a pulsed-laser diode (Toptica) and focused into a 1.4-NA objective lens (PL APO, $\times 100$, oil, Leica). Collected by the same lens, the fluorescence was separated from the laser beams by a custom-made dichroic mirror; it was then filtered via a 525/60 bandpass filter and imaged onto a multimode optical fiber with an opening that features a diameter corresponding to 0.78 of the back-projected Airy disk, serving as confocal pinhole. The pulses for STED were delivered by a Ti:sapphire laser (MaiTai, Spectra-Physics) operating at 80 MHz and emitting at $\lambda = 795 \text{ nm}$, which was then converted to $\lambda = 595 \text{ nm}$ by using an optical parametric oscillator (APE). The resulting pulses of 200-fs length were coupled into a polarization-preserving fiber (OZ Optics) of 120-m length to improve the spatial profile and stretch the pulses by dispersion to $\approx 300 \text{ ps}$. The excitation pulses were synchronized with the STED pulses via external triggering of the laser diode; the delay was tuned with a home-built electronic delay generator. The expanded STED beam was split into two paths and merged at two polarizing beam splitters. The ratio of the two paths could be adjusted by rotation of the polarization via a half-wave plate. In each path the beam passed through a phase plate introducing a phase delay of π in the center to create the z -doughnut or through a polymeric phase plate (RPC Photonics) applying a helical phase ramp of $\exp(i\varphi)$, with $0 < \varphi < 2\pi$ delivering the r -doughnut, respectively. For lateral resolution enhancement, the microscope was operated with the r -doughnut only (Fig. 1B). For axial enhancement, the z -doughnut was overlapped with a slightly expanded r -doughnut (Fig. 1C). The expansion of the r -doughnut was effected by an iris decreasing the beam diameter and, thus, the aperture of the beam; the same measure also slightly elongates the r -doughnut along the z axis (Fig. 1C). All recordings of the ER were performed with a piezostage scanner (P-733, Physik Instrumente); the microtubules were recorded with resonant mirror scanning (15 kHz, SC-30, Electro-Optical Products Corp.) along the x axis and stage scanning along the y axis. In the CW version of the STED microscope, the optical elements for preparing and timing of the pulses are obsolete. The CW excitation and STED beams were provided by CW lasers of the appropriate wavelengths as described in Results. The STED beam passed the same polymeric phase plate as in the pulsed case delivering an equivalent r -doughnut in the focal plane.

DNA Constructs. For the plasmids targeting the fluorescent protein to the ER, the coding regions of Citrine and EYFP, respectively, were amplified by PCR using the primers CTGCAGGTCGACATGGTGAGCAAGGGCGAGGA and TTCT-GCGGCCCTGTACAGCTGCTCCATGCCCGCGT and ligated into pEF/myc/ER (Invitrogen) by using Sall and NotI restriction sites. Citrine-Tubulin is based on pEGFP-Tub (Clontech Laboratories), in which Citrine was substituted for EGFP by using NheI and BglII and the primers GATCCGCTAGCGCTAATGGTGAG-CAAGGGCGAGGAG and CACTCGAGATCTGAGTCCGGACTGTACAGCT-CGTCATGC.

After amplification, DNA was purified by using the Endofree Plasmid Maxi kit (Qiagen).

Cell Culture and Transfection. PtK2 (potoroo kidney) cells were cultured in DMEM supplemented with 5% FCS, 100 units/ml streptomycin/penicillin (all GIBCO-Invitrogen), and 1 mM pyruvate (Sigma) at 37°C and 7% CO_2 . Twenty-four hours after seeding the cells on cover glasses, they were transfected with endotoxin-free DNA by using Nanofectin (PAA). The cells were incubated for at least 24 h before imaging.

ACKNOWLEDGMENTS. We thank R. Y. Tsien for providing the plasmid coding for Citrine, S. Löbermann, S. Jakobs, and R. Medda for help with the preparation of the samples, J. Jethwa for critical reading, A. Schönle for the analysis software ImSpector, and V. Westphal for help with the scanning system. We also thank the German Ministry for Research and Education (BMBF, Biophotonik III) for support.

1. Tsien RY (1998) The green fluorescent protein. *Annu Rev Biochem* 67:509–544.
2. Pawley JB, ed (2006) *Handbook of Biological Confocal Microscopy* (Springer, New York).
3. Abbe E (1873) Contributions to the theory of the microscope and the microscopical perception (Translated from German). *Arch Mikr Anat* 9:413–468.
4. Hell SW, Wichmann J (1994) Breaking the diffraction resolution limit by stimulated emission: Stimulated emission depletion microscopy. *Opt Lett* 19:780–782.
5. Klar TA, Jakobs S, Dyba M, Egner A, Hell SW (2000) Fluorescence microscopy with diffraction resolution limit broken by stimulated emission. *Proc Natl Acad Sci USA* 97:8206–8210.
6. Hell SW (2007) Far-field optical nanoscopy. *Science* 316:1153–1158.
7. Westphal V, Hell SW (2005) Nanoscale resolution in the focal plane of an optical microscope. *Phys Rev Lett* 94:143903.
8. Hofmann M, Eggeling C, Jakobs S, Hell SW (2005) Breaking the diffraction barrier in fluorescence microscopy at low light intensities by using reversibly photoswitchable proteins. *Proc Natl Acad Sci USA* 102:17565–17569.
9. Betzig E, et al. (2006) Imaging intracellular fluorescent proteins at nanometer resolution. *Science* 313:1642–1645.
10. Rust MJ, Bates M, Zhuang X (2006) Sub-diffraction-limit imaging by stochastic optical reconstruction microscopy (STORM). *Nat Methods* 3:793–796.
11. Hess ST, Girirajan TPK, Mason MD (2006) Ultra-high resolution imaging by fluorescence photoactivation localization microscopy. *Biophys J* 91:4258–4272.
12. Willig KI, et al. (2006) Nanoscale resolution in GFP-based microscopy. *Nat Methods* 3:721–723.
13. Huang B, Wang W, Bates M, Zhuang X (2008) Three-dimensional super-resolution imaging by stochastic optical reconstruction microscopy. *Science* 319:810–813.
14. Fölling J, et al. (2007) Photochromic rhodamines provide nanoscopy with optical sectioning. *Angew Chem Int Ed* 46:6266–6270.
15. Shroff H, Galbraith CG, Galbraith JA, Betzig E (2008) Live-cell photoactivated localization microscopy of nanoscale adhesion dynamics. *Nat Methods* 5:417–423.
16. Westphal V, et al. (2008) Video-rate far-field optical nanoscopy dissects synaptic vesicle movement. *Science* 320:246–249.
17. Griesbeck O, Baird GS, Campbell RE, Zacharias DA, Tsien RY (2001) Reducing the environmental sensitivity of yellow fluorescent protein: Mechanism and applications. *J Biol Chem* 276:29188–29194.
18. Denk W, Strickler JH, Webb WW (1990) Two-photon laser scanning fluorescence microscopy. *Science* 248:73–76.
19. Hopt A, Neher E (2001) Highly nonlinear photodamage in two-photon fluorescence microscopy. *Biophys J* 80:2029–2036.
20. Willig KI, Harke B, Medda R, Hell SW (2007) STED microscopy with continuous wave beams. *Nat Methods* 4:915–918.